3D simulations of M star atmosphere velocities and their influence on molecular FeH lines

S. Wende[1], A. Reiners[1], and H.-G. Ludwig[2]

[1] Institut für Astrophysik, Georg-August-Universität Göttingen, Friedrich-Hund Platz 1, D-37077, Germany
e-mail: `sewende@astro.physik.uni-goettingen.de` e-mail: `Ansgar.Reiners@phys.uni-goettingen.de`
[2] GEPI, CIFIST, Observatoire de Paris-Meudon, 5 place Jules Janssen, 92195 Meudon Cedex, France
e-mail: `Hans.Ludwig@obspm.fr`

ABSTRACT

Context. The measurement of line broadening in cool stars is in general a difficult task. In order to detect slow rotation or weak magnetic fields, an accuracy of $1\,\mathrm{km\,s^{-1}}$ is needed. In this regime the broadening from convective motion become important. We present an investigation of the velocity fields in early to late M-type star hydrodynamic models, and we simulate their influence on FeH molecular line shapes. The M star model parameters range between $\log g$ of $3.0 - 5.0$ and effective temperatures of 2500 K and 4000 K.
Aims. Our aim is to characterize the T_{eff}- and $\log g$-dependence of the velocity fields and express them in terms of micro- and macro-turbulent velocities in the one dimensional sense. We present also a direct comparison between 3D hydrodynamical velocity fields and 1D turbulent velocities. The velocity fields strongly affect the line shapes of FeH, and it is our goal to give a rough estimate for the $\log g$ and T_{eff} parameter range in which 3D spectral synthesis is necessary and where 1D synthesis suffices. Eventually we want to distinguish between the velocity-broadening from convective motion and the rotational- or Zeeman-broadening in M-type stars which we are planning to measure. For the latter FeH lines are an important indicator.
Methods. In order to calculate M-star structure models we employ the 3D radiative-hydrodynamics (RHD) code CO⁵BOLD. The spectral synthesis on these models is performed with the line synthesis code LINFOR3D. We describe the 3D velocity fields in terms of a Gaussian standard deviation and project them onto the line of sight to include geometrical and limb-darkening effects. The micro- and macro-turbulent velocities are determined with the "Curve of Growth" method and convolution with a Gaussian velocity profile, respectively. To characterize the $\log g$ and T_{eff} dependence of FeH lines, the equivalent width, line width, and line depth are regarded.
Results. The velocity fields in M-stars strongly depend on $\log g$ and T_{eff}. They become stronger with decreasing $\log g$ and increasing T_{eff}. The projected velocities from the 3D models agree within $\sim 100\,\mathrm{m\,s^{-1}}$ with the 1D micro- and macro-turbulent velocities. The FeH line quantities systematically depend on $\log g$ and T_{eff}.
Conclusions. The influence of hydrodynamical velocity fields on line shapes of M-type stars can well be reproduced with 1D broadening methods. FeH lines turn out to provide a mean to measure $\log g$ and T_{eff} in M-type stars. Since different FeH lines behave all in a similar manner, they provide an ideal measure for rotational and magnetic broadening.

Key words. line: profiles - stars: low-mass, brown dwarfs - Hydrodynamics - Turbulence

1. Introduction

Most of our knowledge about stars comes from spectroscopic investigation of atomic or molecular lines. In sun-like and hotter stars, the strength and shape of atomic spectral lines provides information on atmospheric structure, velocity fields, rotation, magnetic fields, etc. Measuring the effects of velocity fields on the shape of spectral lines requires a spectral resolving power between $R \sim 10,000$ ($\Delta v = 30\,\mathrm{km\,s^{-1}}$) for rapid stellar rotation, $R \gtrsim 30,000$ ($\Delta v = 10\,\mathrm{km\,s^{-1}}$) for slower rotation and high turbulent velocities, and resolution on the order of $R \sim 100,000$ for the analysis of Zeeman splitting and line shape variations due to slow convective motion.

In slowly rotating sun-like stars, usually a large number of relatively isolated spectral lines are available for the investigation of Doppler broadened spectral lines. These lines are embedded in a clearly visible continuum allowing a detailed analysis of individual lines at high precision. At cooler temperature, first the number of atomic lines is increasing so that more and more lines become blended rendering the investigation of individual lines more difficult. At temperatures around 4000 K, molecular lines, predominantly VO and TiO, start to become important. At optical wavelengths, molecular bands in general consist of many lines that are blended so that the absorption mainly appears as an absorption band; individual molecular lines are difficult to identify. At temperatures in the M type stars regime (4000 K and less), atomic lines start to vanish because atoms are mainly neutral and higher ionization levels are weakly populated. Only alkali lines appear that are strongly affected by pressure broadening. Thus, the detailed spectroscopic investigation of velocity fields in M dwarfs is very difficult at optical wavelengths.

M-type stars emit the bulk of their flux at infrared wavelengths redward of $1\,\mu$m. This implies that observation of high SNR spectra in principle is easier in the infrared. Furthermore, M type stars exhibit a number of molecular absorption bands in the infrared, for example FeH. In these bands, the individual lines are relatively well separated and provide a good tracer of stellar velocity fields. The lines are intrinsically much narrower than atomic lines in sun-like stars because Doppler broadening due to the temperature related motion of the atoms and molecules is much reduced. Thus, the lines can be used for the whole arse-

nal of line profile analysis that has been applied successfully to sun-like stars over the last decades.

Examples of analyses using FeH lines are the investigation of the rotation activity connection in field M-dwarfs, which requires the measurement of rotational line broadening with an accuracy of $1 \, \mathrm{km \, s^{-1}}$ (Reiners 2007). Another example is the measurement of magnetic fields comparing Zeeman broadening in magnetically sensitive and insensitive absorption lines (see e.g. Reiners & Basri 2006). A precise analysis of FeH lines, however is only possible if the underlying velocity fields of the M dwarfs atmospheres are thoroughly understood. In this paper, we model the surface velocity fields of M type stars and their influence on the narrow spectral lines of FeH.

We calculate 3D-CO^{5}BOLD structure models (Ludwig et al. 2002) which serve as an input for the line formation program LINFOR3D (based on Baschek et al. 1966). Turbulence's are included in a natural way using hydrodynamics, so that we are able to investigate the modeled spectral lines for effects from micro- and macro-turbulent velocities in the classical sense and their influence on the line shapes. The comparison with 1D-models gives a rough estimate of the necessity of using 3D-models in the spectral domain of cool stars. In the first part of this paper we investigate the velocity fields in the models and their dependence on $\log g$ and T_{eff}. In the second part, we investigate the influence of velocity fields, $\log g$, and T_{eff} on the FeH molecular lines.

2. 3D model atmospheres

The three-dimensional time-dependent model atmospheres (hereafter "3D models") are calculated with the radiation-hydrodynamics code CO^{5}BOLD (abbreviation for "COnservative COde for the COmputation of COmpressible COnvection in a BOx of L Dimensions with L=2,3"). It is designed to model solar and stellar surface convection. For solar-like stars like the M-type objects considered here, CO^{5}BOLD employs a local set-up in which the governing equations are solved in a small (relative to the stellar radius) Cartesian domain located at the stellar surface ("box in a star set-up"). The optically thin stellar photosphere and the upper-most part of the underlying convective envelope are embedded in the computational domain. CO^{5}BOLD solves the coupled non-linear equations of compressible hydrodynamics in an external gravitational field in three spatial dimensions (Freytag et al. 2002; Wedemeyer et al. 2004) together with non-local frequency-dependent radiative transfer. In these 3D models convection is treated without any assumptions like in 1D mixing-length theory. The velocity fields and its related transport properties are a direct result of the solution of the hydrodynamic equations. Due to this, CO^{5}BOLD is a well-suited tool to investigate the influence of velocity fields on spectral line shapes. A CO^{5}BOLD model consists of a sequence of 3D flow fields ("snapshots") representing the temporal evolution and spatial structure of the flow. To perform spectral synthesis calculations based on the 3D CO^{5}BOLD-models we use the 3D line formation code Linfor3D. It takes into account the full 3D thermal structure and velocity field in the calculation of the line profiles. It assumes strict Local Thermodynamic Equilibrium (LTE). In this paper we will call the spectral lines computed from three-dimensional atmosphere models "3D-lines".

In order to analyze the influence of velocity fields in M-stars on FeH lines, we construct a set of CO^{5}BOLD-models with $T_{\mathrm{eff}} = 2500 \, \mathrm{K} - 4000 \, \mathrm{K}$ and $\log g = 3.0 - 5.0$ [cgs]. Table 1 give the model parameters. In the T_{eff}-sequence, we simulated main sequence stars and varied the surface gravity slightly with in-

creasing effective temperature. For the $\log g$-sequence, we computed models with different $\log g$ values aiming at the same effective temperature of 3300 K but the models settle to slightly higher or lower T_{eff} values. We decided not to adjust these resulting effective temperatures, because slight differences in T_{eff} do not change the line profiles significantly. We accepted the T_{eff} deviations to avoid the large computational effort which would be necessary to adjust the models to a common effective temperature. However, we apply corrections to the line shape related quantities such as equivalent width (see Section 4.3).

The opacities used in the CO^{5}BOLD model calculations originate from the PHOENIX stellar atmosphere package (Hauschildt & Baron 1999) assuming a solar chemical composition according to Asplund et al. (2005). The opacity tables were computed after Ferguson et al. (2005) and Freytag et al. (2009). These opacities are particularly well-suited for our investigation since they are adapted to very cool stellar atmospheres. The raw data consist of opacities sampled at 62,890 wavelength points for a grid of temperatures and gas pressures. For representing the wavelength dependence of the radiation field in the CO^{5}BOLD models the opacities are re-sampled into six wavelength groups using the opacity binning method (Nordlund 1982; Ludwig 1992; Ludwig et al. 1994). In this approach, the frequencies which reach monochromatic optical depth unity within a certain depth range of the model atmosphere, will be grouped into one frequency bin on the basis of their opacities. For each investigated atmospheric parameter combination the sorting of the wavelengths into groups is performed according the run of monochromatic optical depth in a corresponding PHOENIX 1D model atmosphere. The thresholds for the sorting are chosen in logarithmic Rosseland optical depth as $\{+\infty, 0.0, -1.0, -2.0, -3.0, -4.5, -\infty\}$. In each group a switching is done from a Rosseland average in the optically thick regime to a Planck average in the optically thin regime, except for the group representing the largest opacities, where the Rosseland average is used throughout. In this last bin, which describes the optically thick regions, only the Rosseland average is used because the radiative transfer is local and can be described as a diffusive process (Vögler et al. 2004).

The horizontal size of the models provide sufficient space to allow the development of a small number (10–20) of convective cells. Their number has to be large enough to avoid box-size dependent effects, but also small enough that there is a sufficient number of grid points available to resolve each individual cell. The size of the convective cells scales roughly inversely proportional to the surface gravity. Accordingly, the horizontal size of the computational box is set to larger sizes towards lower $\log g$ values. The horizontal size of the model with $T_{\mathrm{eff}} = 3275 \, \mathrm{K}$ is just large enough to fulfill the criteria of the minimal number of 10 convective cells (see Fig. 5), and we saw in test simulations that the results will not change with a larger model (in horizontal size). Therefore we will use this well evolved model as well. The vertical dimension is set to embed the optically thin photosphere, and a number of pressure scale heights of the sub-photospheric layers below. We deliberately keep the depth of our models rather small to avoid problems due to numerical instabilities analogous to the ones encountered and discussed in our previous works on the hydrodynamics of M-type stellar atmospheres (Ludwig et al. 2002, 2006).

For the comparison with 1D models, we spatially average the 3D-model over surfaces of equal Rosseland optical depth at selected instants in time. We call the obtained sequence of 1D structures ⟨3D⟩-model. We follow the procedure of Steffen et al. (1995) and average the fourth moment of the temperature and

Table 1. Overview of different model quantities for models at constant T_{eff} and different $\log g$ (upper part) and at constant $\log g$ and different T_{eff} (lower part).

Model code	Size(x,y,z) [km]	Grid points (nx,ny,nz)	H_p [km][a]	z-size [H_p]	T_{eff} [K]	$\log g$ [cgs]
d3t33g30mm00w1	85000 x 85000 x 58350	180 x 180 x 150	2821	20.7	3240	3.0
d3t33g35mm00w1	28000 x 28000 x 11500	180 x 180 x 150	826	13.9	3270	3.5
d3t33g40mm00w1	7750 x 7750 x 1850	150 x 150 x 150	250	7.4	3315	4.0
d3t33g50mm00w1	300 x 300 x 260	180 x 180 x 150	18	14.5	3275	5.0
d3t40g45mm00n01	4700 x 4700 x 1150	140 x 140 x 141	109	10.6	4000	4.5
d3t38g49mm00w1	1900 x 1900 x 420	140 x 140 x 150	36	11.7	3820	4.9
d3t35g50mm00w1	1070 x 1070 x 290	180 x 180 x 150	20	14.5	3380	5.0
d3t28g50mm00w1	370 x 370 x 270	250 x 250 x 140	13	20.8	2800	5.0
d3t25g50mm00w1	240 x 240 x 170	250 x 250 x 120	12	14.2	2575	5.0

[a] at $\tau = 1$

first moment of the gas pressure to preserve the radiative properties of the 3D-model as far as possible. The 3D velocity information is ignored in the ⟨3D⟩-model and replaced by a micro- and macro-turbulent velocity. By construction, the ⟨3D⟩-model has the same thermal profile as the 3D-model, but evidently without the horizontal inhomogeneities related to the convective granulation pattern. We will call the spectral lines synthesized from ⟨3D⟩-models "⟨3D⟩-lines".

2.1. Atmosphere structures

The temperature stratification shown in Fig.1 (top left) of the models with changing T_{eff} appears very similar for all models in the region below $\log \tau \sim 1$. They reach their T_{eff} around $\tau \sim 2/3$ and continue to decrease to higher atmospheric layers. Above $\log \tau \sim 1$ the temperature of the two hottest models increase more strongly than in the cooler cases. Since the models are almost adiabatic in the deeper layers (see below) the temperature gradient follows the adiabatic gradient, which is given by the equation of state and steeper in hotter models due to the inefficient H_2 molecule formation. This increase of temperature is also very similar to the lower $\log g$ models on the right side of Fig.1. These models also show a temperature gradient which becomes steeper to deeper atmospheric layers and with decreasing surface gravity again due to a steeper adiabatic gradient. All models reach an almost equal effective temperature at $\tau \sim 2/3$ and their temperature stratification does not differ strongly to smaller optical depth.

The entropy stratification for models with varying T_{eff} (mid left in Fig.1) show a similar behavior for all models. It is adiabatic ($dS/d\tau = 0$) in layers below $\log \tau \sim 1$ and has a superadiabatic region ($dS/d\tau > 0$) between $\log \tau \sim 1$ and ~ -1 that moves slightly to smaller optical depth for hotter models. In these regions, with $dS/d\tau \geq 0$, the models are convectively unstable and become convectively stable in the outer parts of the atmosphere where $dS/d\tau < 0$. In the models with changing $\log g$ (mid right in Fig.1), we can see that the entropy behaves almost like in the T_{eff} case. To lower surface gravities, the superadiabatic region is more significant. In higher layers, the models become convectively stable except the model with $\log g = 4.0$ [cgs] which shows a second decrease of entropy to the outer part layers. To understand this behavior, we have to investigate the adiabatic gradient of this region which is very small and changes very little along the upper atmosphere. This is due to the equation of state used in the models and can be seen in Fig.16 of Ludwig et al. (2006) (model H4 in this figure equates to our $\log g = 4.0$ model). This figure shows that the upper atmosphere lies in a plane of small and constant adiabatic

gradient. Due to this, the model becomes convectively unstable again in the upper layers. This is probably the reason for the, in comparison to other models, higher velocities in this model.

In the left bottom panel of Fig.1, the horizontal and vertical rms-velocities are plotted for models with different T_{eff}. Both velocity components increase with increasing T_{eff}. The maxima of the vertical velocity moves to slightly deeper layers with higher temperatures and the maxima of the horizontal velocity stays almost at the same optical depth. We can see a qualitatively similar dependence in the $\log g$ model sequence in the right bottom plot in Fig.1. Only the model with $\log g = 4.0$ [cgs] shows peculiar behavior in the upper atmospheric layers, which is probably related to the entropy stratification in this model. We will describe the velocity fields in the models in more detail and with a slightly different method in the next section.

3. Velocity fields in the CO⁵BOLD-models

Before we investigate the effect of velocity fields on spectral lines, we analyze the velocity fields in the models themselves and we will do this with respect to spectral lines. Spectral lines are broadened by velocity fields where the wavelength of absorption or emission of a particle is shifted due to its motion in the gas. Here we are mostly concerned with the macroscopic, hydrodynamic motions but have in mind that the thermal motions are also constituting an important contribution. If we envision each voxel in the RHD model cube to form its own spectral line, the whole line consists of a (weighted) sum of single lines. The velocity distribution might be represented by a histogram of the velocities of the voxels which gives us the velocity dispersion. We try to describe the velocity fields in that sense instead of using the rms-velocities shown in Fig.1. In the CO⁵BOLD-models, a velocity vector is assigned to each voxel and consists of the velocities in x-, y-, and z-direction. We will investigate the vertical and horizontal component of the velocity dispersion in the models and the total velocity dispersion $\sigma_{tot} = \sqrt{\sigma_x^2 + \sigma_y^2 + \sigma_z^2}$. In order to describe the height dependent velocity dispersion we applied a binning method, i.e. we plot all velocity components of a certain horizontal plane of equal optical depth τ in the CO⁵BOLD cube in a histogram with a bin size of $25 \, \mathrm{m \, s^{-1}}$. We fit the histogram velocity distribution with a Gaussian normal distribution function $G = \exp{(-(\frac{x}{\sigma})^2)}$ and take the standard deviation σ as a measure for the velocity dispersion σ in the models (see Fig. 2) (The relation between the Gaussian standard deviation σ and the standard deviation σ_{rms} of the mean velocity is $\sigma = \sqrt{2} \cdot \sigma_{rms}$). This is done for the σ_x, σ_y, and σ_z component of the velocity vector for each horizontal plane from τ_{min} to τ_{max}, which are the highest
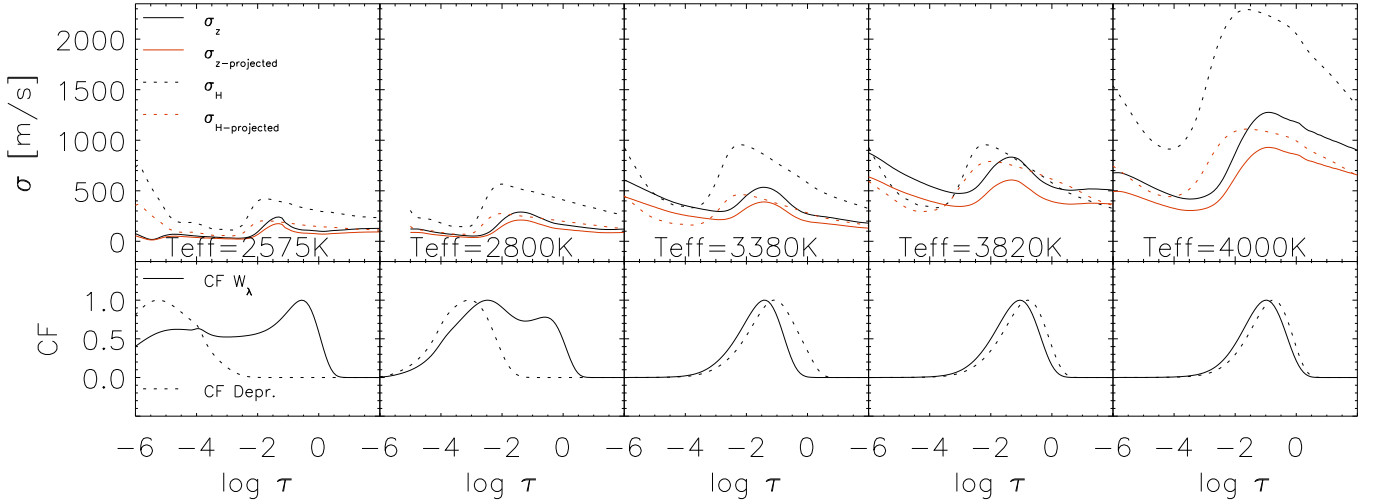
Fig. 3. Upper panel: Radial (σ_z) and horizontal (σ_H) components of the velocity dispersion are plotted against the optical depth on a logarithmic scale. Bottom panel: Each bottom panel shows the contribution functions (CF) of an FeH-line at a wavelength of 9956.72 Å. Equivalent width W_λ (solid) and the depression at the line center (dashed) of the line are plotted as a function of optical depth on a logarithmic scale. The models (from left to right) are located at T_{eff} of 2800 K, 3380 K, 3820 K and 4000 K and a log g value of 5.0, except the one with T_{eff} = 3820 K (log g = 4.9), and the one with T_{eff} = 4000 K (log g = 4.5) [cgs].
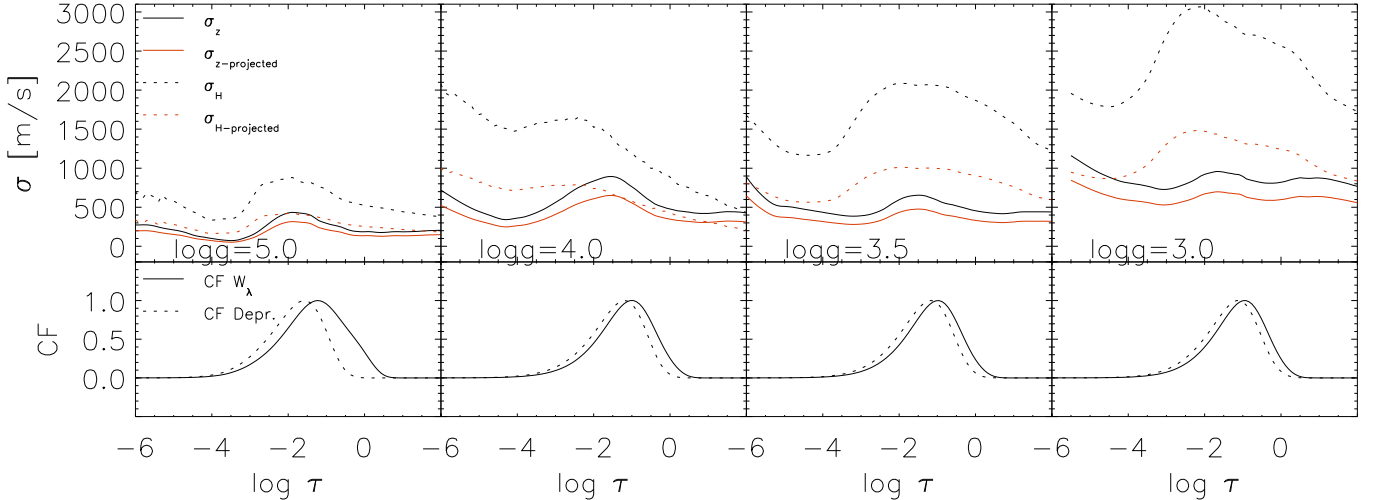
Fig. 4. Upper panel: Radial (σ_z) and horizontal (σ_H) components of the velocity dispersion are plotted against the optical depth on a logarithmic scale. Bottom panel: Each bottom panel shows the contribution functions (CF) of an FeH-line at a wavelength of 9956.72 Å. Equivalent width W_λ (solid) and the depression at the line center (dashed) of the line are plotted as a function of optical depth on a logarithmic scale. The models are located at log g values from left to right of 5.0 (T_{eff} = 3275 K), 4.0 (T_{eff} = 3315 K), 3.5 (T_{eff} = 3270 K) and 3.0 (T_{eff} = 3240 K) [cgs].

and the deepest points, in each model atmosphere. In this way we obtained the height dependent velocity dispersion $\sigma_{x,y,z}(\tau)$. We average over five model snapshots for a better statistical significance. In Figs. 3 and 4, the velocity dispersions for the horizontal components $\sigma_H = \sqrt{\sigma_x^2 + \sigma_y^2}$ and vertical component σ_z are plotted against optical depth (black solid and dotted lines). In the latter figures, we identify the maxima around $\log \tau = -1$ of the velocity dispersions as the region where the up-flowing motion spreads out in horizontal direction and starts to fall back to deeper layers. We will call this point, the "convective turn-over point". In a horizontal 2D cross-section of the vertical velocities, somewhat below this area, the up-flowing granulation patterns are clearly visible (see Fig.5 for models with different

log g or Ludwig et al. (2006)). In a vertical 2D cross-section one can see the behavior of the up-streaming material (Fig. 6 shows an example for a model with T_{eff} = 2800 K). The material starts moving upwards almost coherently and before reaching higher layers (around z = 200 km in Fig. 6) of the atmosphere the vertical velocity dispersion σ_z becomes maximal. After that point, the material spreads out in horizontal directions and starts falling down again. At this point, the dispersion of horizontal velocities σ_H becomes maximal (convective turn-over point).

In Fig.4 we can see at lower surface gravities that the maxima of the horizontal velocity dispersion are not centered around a specified optical depth anymore; it spreads out in vertical direction and span the widest range at log g = 3.0 [cgs]. The pressure
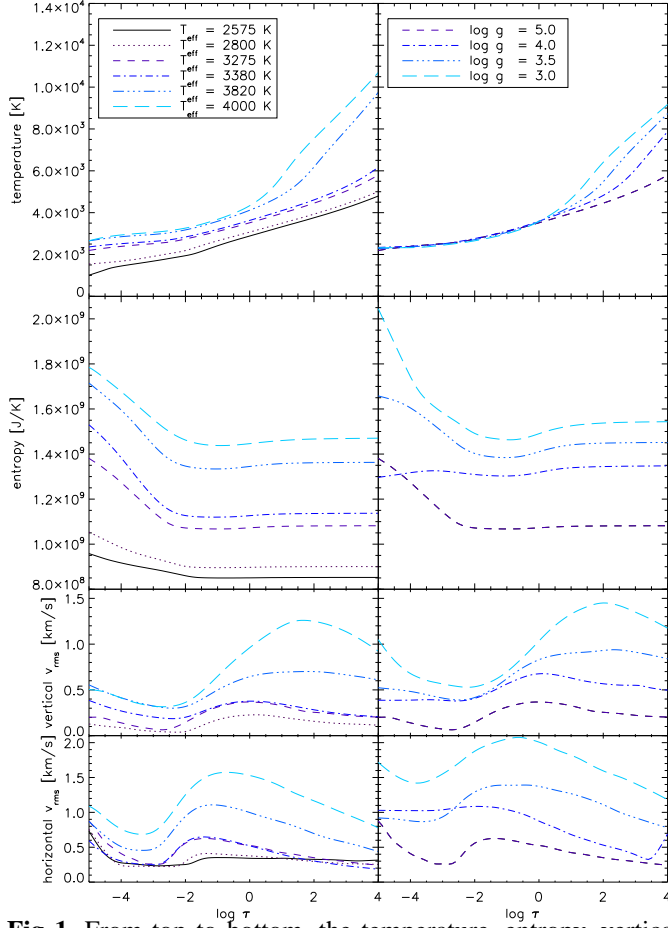
Fig. 1. From top to bottom, the temperature, entropy, vertical, and horizontal velocity are plotted as a function of optical depth. The column on the left side shows models with different T_{eff} and constant $\log g$, on the right side the models are at a constant T_{eff} with varying $\log g$. The rise of horizontal velocity in the $\log g = 4.0$ [cgs] model in the deeper atmospheric layers is due to interpolation from z- to τ-scale.
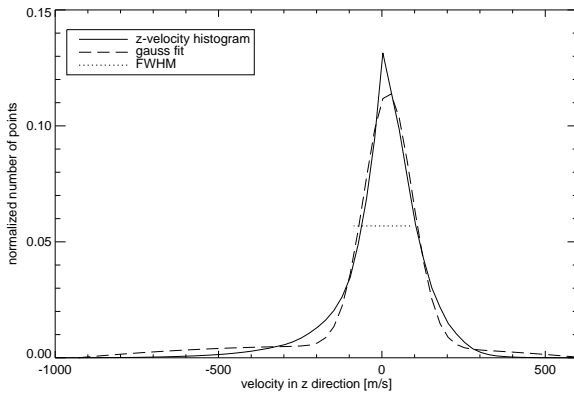
Fig. 2. Histogram of the velocity distribution in vertical direction. The normalized number of points is plotted against the vertical velocity in m/s (solid line). The Gaussian (dashed line) fits the velocity distribution and determined an FWHM value (dashed-dotted line), which is related to σ with $FWHM = 2\sqrt{\ln 2} \cdot \sigma$. The underlying model is located at $T_{\mathrm{eff}} = 2800\,\mathrm{K}$ and $\log g = 5$ [cgs].
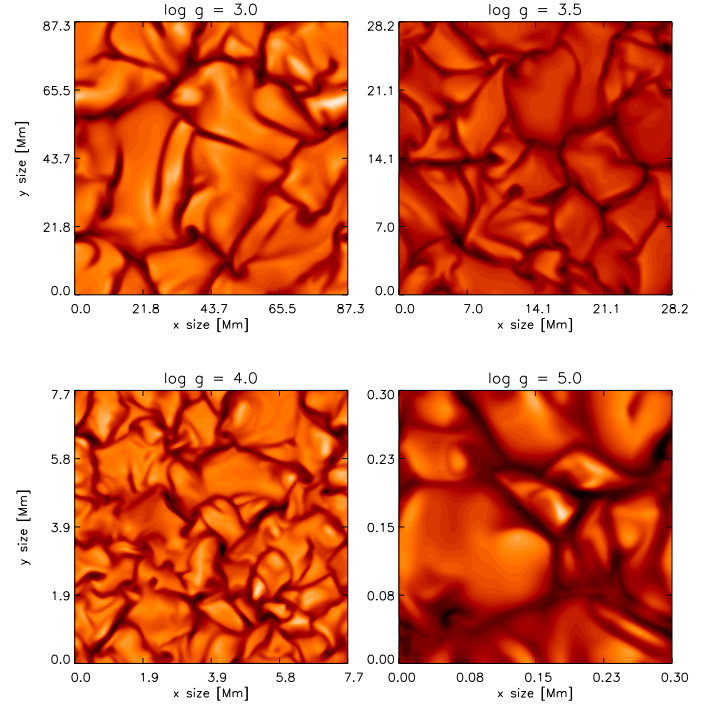
Fig. 5. Horizontal cross-section around $\tau \sim 1$ of vertical velocity components. The models are located at $\log g$ values of 3.0, 3.5, 4.0, and 5.0 [cgs] (from upper left corner to lower right, respectively).
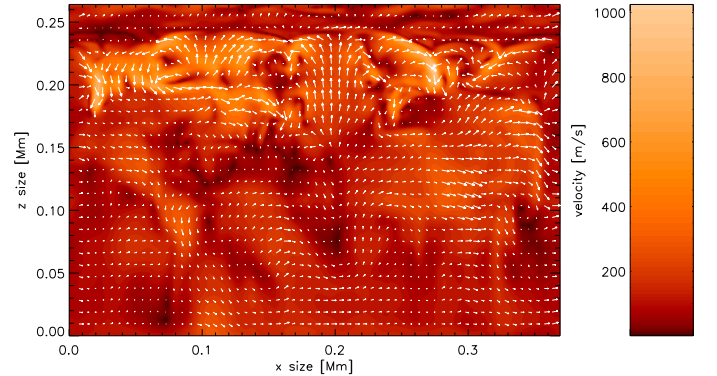

Fig. 6. 2D cross-section in x-z direction of the x-z velocity in a model with $\log g = 5.0$ [cgs] and $T_{\mathrm{eff}} = 2800\,\mathrm{K}$. Overplotted are x-z velocity vectors. The direction of the material flow is indicated by the velocity vectors.

stratification changes, and the convective turn-over point moves to lower gas-pressure (not shown here) but stays at almost constant optical depth between $\log \tau = 0$ and $\log \tau = -2$. With varying temperature, the position of the convective turn-over point stays at almost constant optical depth.

3.1. Reduction of the 3D velocity fields

Commonly, micro- and macro-turbulence derived from spectroscopy are interpreted as being associated with actual veloc-
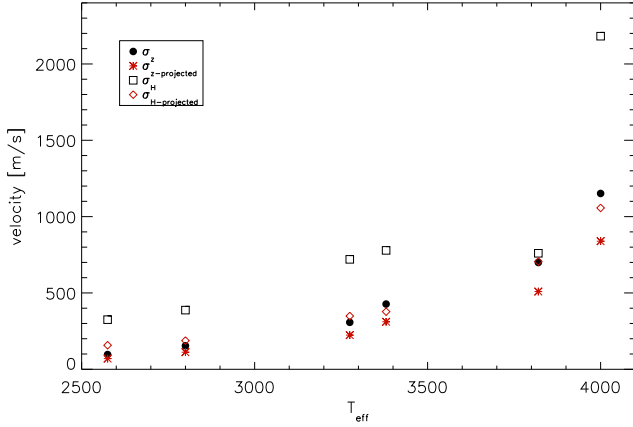
Fig. 7. Plotted are the weighted projected and unprojected velocity dispersions of the horizontal and vertical component for models with different $T_{\rm eff}$. The models are located at $T_{\rm eff}$ values of 2575 K, 2800 K, 3275 K, 3380 K, 3820 K and 4000 K and a log g value of 5.0, except the one with $T_{\rm eff}$ = 3820 K (log g = 4.9), and the one with $T_{\rm eff}$ = 4000 K (log g = 4.5) [cgs].
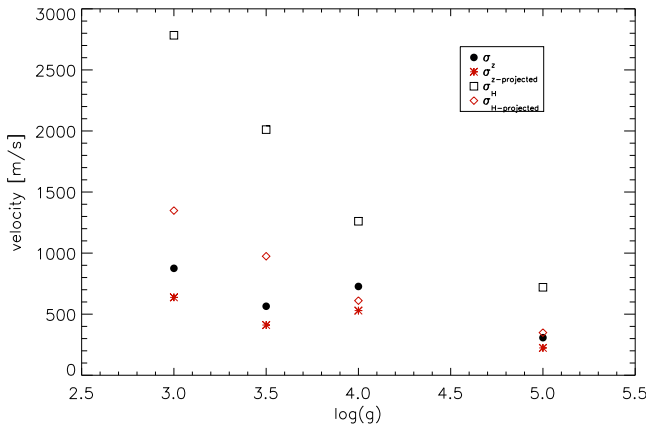
Fig. 8. Plotted are the weighted projected and unprojected velocity dispersions of the horizontal and vertical component for models with different log g. The models are located at $T_{\rm eff}$ around 3300K and different log g values of 3.0 ($T_{\rm eff}$ = 3240 K), 3.5 ($T_{\rm eff}$ = 3270 K), 4.0 ($T_{\rm eff}$ = 3315 K) and 5.0 ($T_{\rm eff}$ = 3275 K) [cgs].

ity fields present in the stellar atmosphere. In our simulations no oscillations are induced externally but small oscillations are generated in the simulations itself. The velocity amplitudes of these oscillations reach maximal 10 % of the convective velocities and have no significant influence on the macro-turbulent velocity. We would also not expect global oscillations for these objects, except for young stars with solar masses smaller than 0.1 $M_{\odot}$ induced by D-burning (Palla & Baraffe 2005). In the following, we try to make the connection between micro- and macro-turbulence and actual hydrodynamical velocity fields manifest by considering the velocity dispersion determined directly from the hydrodynamical model data, and compare it with the micro- and macro-turbulence derived from synthesized spectral lines (see Sec.3.2). This connection is algebraically not immediate, and we only apply a simple model for translating the hydrodynamical velocities into turbulent velocities relevant to spec-

troscopy (see appendix). When interpreting comparisons shown below the very approximate nature of our model should be kept in mind. In this model, we include the geometrical projection of the components of $\sigma_{x,y,z}$ to the line of sight of the observer. We also have to consider the effect of limb-darkening of the stellar disk. For each velocity dispersion component we calculate a projection factor which includes both, geometrical projection and limb-darkening effects (more described in the appendix). We take a limb-darkening coefficient of 0.4 which follows from the continuum from angle dependent line synthesis performed in LINFOR3D. These simulations suggest that a linear limb-darkening law with a limb-darkening coefficient of 0.4 is suited to describe the brightness variation. The projected velocity dispersions are also plotted in Figs. 3 and 4 (red solid and dotted lines). The reducing effect of this projection factor is stronger in the horizontal components than in the vertical because the projected area at the limb of the stellar disk, where σ_H reaches its maximum value, is much smaller than in the center where σ_z has its maximum value. The influence of limb-darkening is not strong and the dependence of the projection factor from the limb-darkening coefficient is only small (described in more detail in the appendix).

3.1.1. Weighted velocities

To investigate the influence of broadening from the projected and unprojected velocity dispersion on spectral lines, we use contribution functions for the equivalent width W_λ and the depression at the line center of an FeH line at 9956.7 Å (Magain 1986). The line gains its W_λ and depression in the region between $\log \tau$ = 1.0 and $\log \tau$ = − 4.0, i.e. that is the region of main continuum absorption caused by FeH molecules. The maximum is roughly centered around $\log \tau$ = − 1.0 and moves to slightly lower optical depth with lower temperatures (at the lowest $T_{\rm eff}$ of 2575 K, the maximum is centered around $\log \tau$ = − 2.0) or higher surface gravities. The contribution function of W_λ range over the region of the convection zone and reflects its influence on the line shape. Due to the latter fact, FeH lines are a good mean to explore the convective regions in M-dwarfs. In order to measure the velocities in the region where the lines originate, we compute the mean of the (projected) velocities weighted with the contribution function of W_λ.

$$\sigma_{\rm weighted} = \frac{\sum_{\tau=2}^{-6} \sigma_\tau \cdot CF_\tau}{\sum_{\tau=2}^{-6} CF_\tau} \tag{1}$$

The horizontal and vertical components of these weighted velocity dispersions are plotted in Figs. 7 and 8. We can see an increase of $\sigma_{H,z}$ with increasing effective temperature or decreasing surface gravity. We can see again that the projected horizontal velocity dispersions are significantly smaller than the unprojected ones due to the reasons mentioned above. The difference in the vertical component is much smaller. The velocity dispersions for the vertical component range from a few hundred m/s for cool, high gravity models to ∼ 1 km s^{-1} for hot or low gravity models. The horizontal component range from a ∼ 500 m s^{-1} for cool, high gravity models to ∼ 2 km s^{-1} for hot or low gravity models. We compare the total projected velocity dispersion $\sigma_{tot} = \sqrt{\sigma_H^2 + \sigma_z^2}$ in Sec. 3.2 with micro- and macro-turbulent velocities in the classical sense.

The strong increase of the velocity dispersions in the atmospheres to higher layers (Figs. 3 and 4), which some models show, is related to convective overshoot into formally stable lay-

ers. These velocities are originated by waves excited by stochastical fluid motions and by advective motions (Ludwig et al. 2002, and references therein). However, it will not affect the spectral lines, because the lines are generated in the region between an optical depth of $\log \tau = 1.0$ and $\log \tau = -4.0$. The lines on the model with $T_{\text{eff}} = 2575\,\text{K}$ are an exception, they are formed in the outermost layers of the model and it is not possible to compute the full range of formation of these lines, because the atmosphere is not extended enough. One has to keep this in mind when regarding the line dependent results of this model later in this chapter.

3.2. Radial velocity shifts

Due to the fact that in a convective motion the up-flowing area is larger, because it is hotter and less dense, than the down-flowing one, one expect a net shift of the velocity distribution to positive velocities. That means, the net amount of up-flowing area with hotter temperature, i.e. more flux in comparison to the down-flowing area, results in a blue shift in the rest wavelength position of a spectral line (see e.g. Dravins 1982).

To see how the area of up-flowing material affects the rest wavelength position of a spectral line, we computed ten FeH spectral lines (more described in Sect. 4) on 3D models to measure the displacement of the line positions. In order to determine the center of the line, we used the weighted mean $C = \frac{\sum F \cdot v}{\sum F}$ which account for the asymmetric line shape. (To use the weighted mean is appropriate here, since we have no noise in the computed data.) The line shifts of the flux and the intensity are given in Tab. 2. A negative value stands for a blue shift, and a positive for a red shift. The values for each model are the mean of five temporal snapshots. The absolute displacement of the flux and intensity in the $\log g$ series reflects the dependence of the velocity fields on surface gravity, but for the T_{eff} series a connection is barely visible (see Figs. 7 and 8). This could be due to the small geometrical size of the atmospheres in the T_{eff} series (see Tab. 1). Only the the one with $T_{\text{eff}} = 4000\,\text{K}$ shows a significant line shift and in this model the atmosphere is 1150 km high due to the slightly smaller $\log g$ value of 4.5 [cgs]. At this point we will not go in deeper analysis of this topic.

Since we only use five snapshots, we are dealing with statistics of small numbers and hence a big scatter in the results. This scatter σ_{shift} is in general one order lower than the shift of the line and the integrated jitter of the line, which is important for radial-velocity measurements, goes with $\sigma_{\text{jitter}} = \frac{\sigma_{\text{shift}}}{\sqrt{N}}$, where N is the number of snapshots. Since in a star N is of the order of 10^6, the jitter will be of the order of $\text{mm\,s}^{-1}$.

We did not further investigate the effect of granulation patterns on the line profiles but, as we will see below, the lines are almost Gaussian and show no direct evidence for significant granulation effects.

3.3. Micro- and macro-turbulent velocities

Due to the large amount of CPU-time required to compute 3D RHD models and spectral lines on these models, we want study the necessity of 3D models in the range of M-stars. Our goal is to compare the broadening effects of the 3D velocity fields on the shape of spectral lines with the broadening in terms of the classical micro- and macro-turbulence profiles (see e.g. Gray 1977, 2008). The latter description is commonly used in 1D atmosphere models like ATLAS9 (Kurucz 1970) or PHOENIX and related line formation codes. If the difference between 1D and 3D velocity broadening is small, the usage of fast 1D atmosphere codes to simulate M-stars for comparisons with observations, e.g. to determine rotational- or Zeeman-broadening, would be an advantage.

If the size of a turbulent element is small compared to unit optical depth, we are in the regime of the micro-turbulence. The micro-turbulent velocities might differ strongly from one position to another and have a statistical nature. The broadening effect on spectral lines can be described with a Gaussian which enters the line absorption coefficient (Gray 2008). It can be treated similar to the thermal Doppler broadening. The effect on the shapes of saturated lines is an enhancement of line wings due to the fact that at higher velocities the absorption cross section increases and as a consequence the equivalent width (W_λ) of the line is increased.
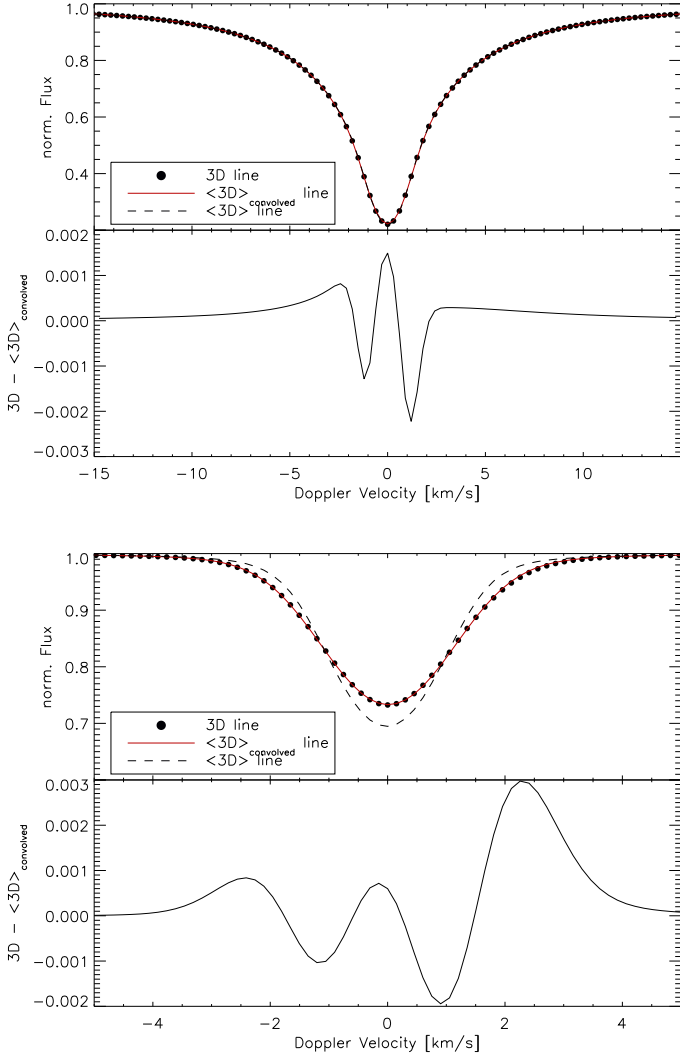
If the size of a turbulent element is large compared to unit optical depth (maybe better of the same size as unit optical depth), we are in the regime of the macro-turbulence. It can be treated similar to rotational broadening as a global broadening of spectral lines. The effect is an increase of the line width but the equivalent width remains constant.

As we saw before, the velocity fields in the M-stars are not very strong in comparison to the sound speed (see Tab.2) and one could expect that their influence on line shapes do not deviate strongly from Gaussian broadening.

We compared line broadening with the radial-tangential profile from Gray (1975) and a simple Gaussian profile and found that the latter is a good approximation with an accuracy high enough for possible determination of rotational- or Zeeman-broadening. Hence, in this investigation we will assume Gaussian broadening profiles. That means, we can assume a height independent isotropic velocity distribution for micro- and macro-turbulent velocities. This is a very convenient way to simulate the velocity fields. One would expect that the anisotropic nature and the height dependence of the hydrodynamical velocity fields have a significant influence on line shapes, so it is remarkable that their influence on spectral lines can be described to a high accuracy in this way. (At least in the investigated M-type stars.) In Fig. 9, a few examples of $\langle 3D\rangle$-FeH spectral lines were plotted, which were computed with a given micro-turbulent velocity (determined below) and then convolved with a Gaussian broadening profile with a given macro-turbulent velocity. The broadened $\langle 3D\rangle$-FeH lines fit the 3D-FeH lines very well. The difference of the 1D and 3D centroid ($C = \frac{\sum F \cdot v}{\sum F}$) range in the order of m/s for small velocity fields to $30 - 40\,\text{m\,s}^{-1}$ for strong velocity fields in hot M star models or with low $\log g$. The error in flux is lower than 1% (see Fig. 9) this corresponds to an uncertainty in velocity, for example rotational velocity, of less than $150\,\text{m\,s}^{-1}$ depending on the position in the line. It is also visible in the latter figures that at low effective temperature effects from velocity broadening are not visible in comparison with an unbroadened $\langle 3D\rangle$-line in which the v.d.Waals broadening is dominant. At higher effective temperatures, the difference between broadened and unbroadened $\langle 3D\rangle$-lines is clearly visible. We found that in the range of M-type stars, 1D spectral synthesis of FeH-lines using micro- and macro-turbulent velocities in the classical description is absolutely sufficient to include the effects of the velocity fields. In the following we will determine the velocities needed.

Table 2. Displacement Δv_{Flux} and $\Delta v_{\text{Intensity}}$ in m/s of the position of an FeH line from the rest wavelength on models with different T_{eff} (left side) and different $\log g$ (right side).

| T_{eff}	Δv_{Flux} [m/s]	$\Delta v_{\text{intensity}}$ [m/s]	v_{ad} [m/s]	$\log g$	Δv_{Flux} [m/s]	$\Delta v_{\text{intensity}}$ [m/s]	v_{ad} [m/s]
2800	0	2	3750	3.0	−56	−25	6100
3275	−1	3	4000	3.5	−47	−36	5500
3380	−2	2	4850	4.0	−16	−7	5400
3820	−1	−5	6000	5.0	−1	3	4500
4000	−44	−28	7000				

Fig. 9. FeH lines for models with T_{eff} = 2800 K, $\log g$ = 5.0 [cgs] (top) and T_{eff} = 3820 K, $\log g$ = 4.9 [cgs] (bottom). The upper panels show the 3D-line (dots) and the $\langle 3D \rangle_{\text{convolved}}$-line (solid line) which was broadened by a Gaussian profile. For comparison we plotted a $\langle 3D \rangle$-line which was not broadened by any velocities (dashed line). In the lower panels the 3D-$\langle 3D \rangle_{\text{convolved}}$ residuals are plotted. One can see the asymmetry which stems from the line shifts due to convective motions. Note the different y-axis scale.

3.3.1. Determination of micro- and macro-turbulent velocities

The investigation of the micro-turbulent velocities was done with the *curve of growth* (CoG) method (e.g., Gray 2008). We artificially increase the line strength of an absorption-line (increase

the $\log gf$ value) which in turn increase the saturation of the line and its influence of the micro-turbulent velocity, which results in an enhancement of W_λ. In order to determine micro-turbulent-velocities, we use Fe I- and FeH-lines produced on $\langle 3D \rangle$-models with different micro-turbulent velocities (there are no differences in micro-turbulent velocities between both types of lines), i.e. for each $\log gf$-value we compute a $\langle 3D \rangle$-line with micro-turbulent velocities between 0 km s^{-1} and 1 km s^{-1} in 0.125 km s^{-1} steps. In this way we obtained CoGs for 9 different micro-turbulent velocities. We compare the equivalent widths in the CoGs with the ones which was computed on the 3D-models and selected the velocity of the CoG which fits the 3D CoG best in the sense of χ^2-residuals. The macro-turbulent velocities are determined by
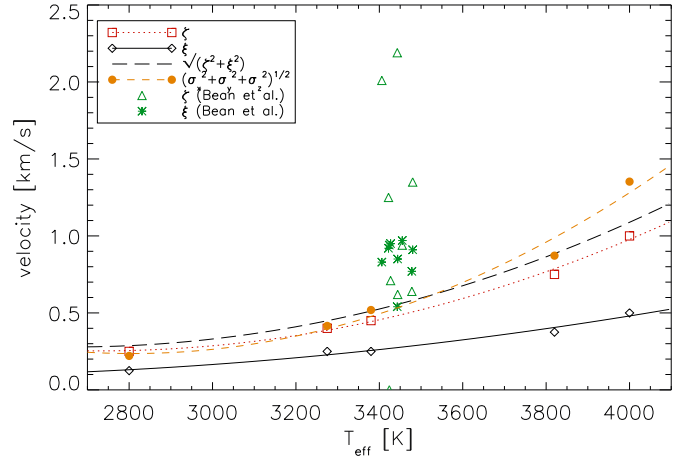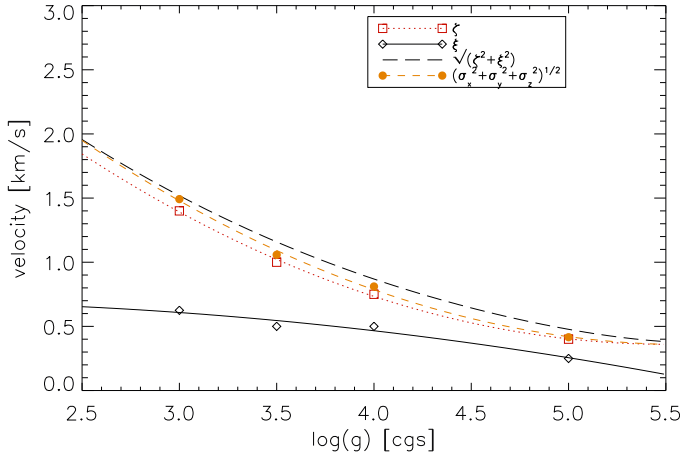

Fig. 10. Macro- (solid) and micro- (dotted) turbulent velocities and the sum of both (long dashed line) as a function of T_{eff}. The data points are fitted by a second order polynomial and the sum of micro- and macro-turbulent velocities is given by the sum of the fits. For comparison, velocities from Bean et al. and the total projected weighted 3D velocity dispersions are plotted, too (short dashed line). The models are located at T_{eff} values of 2800 K, 3275 K, 3380 K, 3820 K and 4000 K and a $\log g$ value of 5.0, except the one with T_{eff} = 3820 K ($\log g$ = 4.9), and the one with T_{eff} = 4000 K ($\log g$ = 4.5) [cgs].

computing a $\langle 3D \rangle$-model FeH line (at λ = 9956.7 Å) including the micro-turbulent velocities. This line is then broadened with a Gaussian profile and different velocities until it matches the 3D-model line.

The dependence of the micro- (ξ) and macro- (ζ) turbulent velocities on surface gravity and effective temperature is plotted in Figs. 10 and 11. The macro-turbulent velocities in both cases show a quadratic dependence, and we can fit them with a second order polynomial. The micro-turbulent velocities could be fitted

Fig. 11. Macro- (solid) and micro- (dotted) turbulent velocities and the sum of both (long dashed line) as a function of $\log g$. The data points are fitted by a second order polynomial and the sum of micro- and macro-turbulent velocities is given by the sum of the fits. For comparison, the total projected weighted 3D velocity dispersions is plotted, too (short dashed line). The models are located at T_{eff} around 3300 K and different $\log g$ values of 3.0 ($T_{\mathrm{eff}} = 3240\,\mathrm{K}$), 3.5 ($T_{\mathrm{eff}} = 3270\,\mathrm{K}$), 4.0 ($T_{\mathrm{eff}} = 3315\,\mathrm{K}$) and 5.0 ($T_{\mathrm{eff}} = 3275\,\mathrm{K}$) [cgs].

by a linear function or a second order polynomial. We decided to use the second order polynomial, too.

Micro- and macro-turbulence velocities both show a similar dependence on surface gravity and effective temperature, which implies that there is a direct connection between both. A comparison of the macro (ζ)- and micro (ξ)-turbulent velocities with the sum of both ($\sqrt{\zeta^2 + \xi^2}$) and the total projected weighted velocity dispersion σ_{tot} (see Sec. 3) is also shown in Figs. 10 and 11. The total projected weighted velocity dispersion (see Sec.3) is very similar to the macro-turbulent velocities and in most cases smaller than the sum of micro- and macro-turbulent velocity. It is remarkably, that it is possible, with this simple description of the total projected weighted velocity, to describe the broadening influence of the hydrodynamical velocity fields on spectral lines in comparison with the classical micro- and macro-turbulent description.

In order to obtain a good estimate of the line profile in 1D spectral line synthesis, knowledge of the micro- and macro-turbulent velocities is very important. Otherwise one could underestimate the equivalent width or the line width and hence obtain a wrong line depth.

We compare our micro- and macro-turbulent velocities to observational results from (see Bean et al. 2006a,b; Bean 2007). Our value of the macro-turbulent velocities are roughly of the same order. The higher macro-turbulent velocities from Bean et al. possibly contain rotational broadening, but the Bean et al. micro-turbulent velocities are roughly a factor two or three higher than ours. These velocities are obtained from observed spectra by the authors of the afore-mentioned papers using spectral fitting procedures. In detail, they used `PHOENIX` atmosphere models and the stellar analysis code `MOOG` (Sneden 1973). One has to keep in mind that the empirical determination of micro-turbulence is also endangered to suffer from systematic errors. For most of the lines that Bean and collaborators employ (line data from Barklem et al. (2000)), the v.d.Waals damping constant is available. However, in some cases not,

then usually Unsöld's hydrogenic approximation is applied to calculate the value, and different authors use significantly different enhancement factors changing its value. This illustrates the level of uncertainty inherent to this approach. For instance, Schweitzer et al. (1996) use an enhance factor of 5.3 (for the resulting γ_6 values) for their Fe I lines, while Bean et al. prefer 2.5 for Ti I lines (Bean 2007). To investigate the detailed influence of v.d.Waals broadening on determination of micro-turbulence velocities is very interesting, but goes beyond the scope of this paper. We want to point out, that it is perceivable that uncertainties in the damping constant can introduce significant systematic biases in the resulting value of spectroscopically micro- and macro-turbulence and they could easily be overestimated.

As mentioned above and illustrated Fig. 10, our prediction of the micro-turbulence grossly underestimates the micro-turbulence values measured by Bean et al.. This might hint at deficits in the hydrodynamical modeling and we cannot exclude the possibility that a process is missing in our 3D models leading to a substantially higher micro-turbulence. But due to the argumentation above and a comparison with the solar micro- and macro-turbulence, we argue that the Bean et al. values for the micro-turbulence are too high. However, before being able to draw definite conclusions the observational basis has to be enlarged.

4. T_{eff}- and $\log g$-dependence of FeH molecular lines

In this section we study the dependence of FeH molecular lines on T_{eff} and $\log g$ in our 3D- and $\langle$3D$\rangle$-models. Again, the intention is to identify multi-D effects which might hamper the use of the FeH line diagnostics in standard 1D analyses. For this purpose we compute the $\langle$3D$\rangle$-lines with no micro- and macro-turbulence velocity. With this method we can study the FeH lines without any velocity effects and can through direct comparison between 3D- and $\langle$3D$\rangle$-lines clearly identify velocity induced effects.

4.1. FeH line data

Wing & Ford (1969) were the first to detect a broad molecular absorption band around 991 nm in late M dwarfs. This band was later found in S stars (Wing 1972) and in sun spots. Nordh et al. (1977) identified the Wing-Ford band as the $0 - 0$ band of a FeH electronic transition. The FeH molecule is well suited for the measurements mentioned in the introduction because of its intrinsically narrow and well isolated spectral lines. These lines are also an ideal tracer of line broadening in M-stars due to convection or very slow rotation (Reiners 2007). Since FeH lines were not very commonly used for the interpretation of stellar spectra in the past, only little data is recorded in the literature. With the work of Dulick et al. (2003), it is possible to determine the $\log gf$ value and the transition energies. For the partition function, a combination of the tabulated function in Dulick et al. (2003) and an analytically determined one from the Eq.1 in Sauval & Tatum (1984) is used.

Due to the high atmospheric pressures, v.d.Waals broadening is often significant in cool M-type dwarfs. No detailed calculations exist for the v.d.Waals broadening of FeH molecular lines. Lacking a more accurate treatment, we follow the approximate approach of Schweitzer et al. (1996) and apply Unsöld's hydrogenic approximation, albeit – different from Schweitzer and coworkers – we do not apply an enhancement factor to the calculated broadening constant C_6.

The ionization energy of the FeH molecule enters the calculation of C_6 which, unfortunately, is not known. Only the dissociation energy is published of 1.59 ± 0.08 eV at 0 K (e.g. Dulick et al. 2003). To derive an estimate of the ionization energy, we heuristically compare the ionization and dissociation energies of a large number of hydrides taking data from Wilkinson (1963). We find an approximately linear relationship between the ionization and the dissociation energies of hydrides. For FeH we obtain an ionization energy of 6 eV for the known dissociation energy from a linear fit. Computation of this value from the ionization-potential of Fe and the dissociation energies of FeH and FeH$^+$ yields 7.3 eV (Bernath 2008, private communication), which is compatible with our value considering our rather crude procedure. The difference in FWHM of synthesized FeH-lines in the range between 6 and 7.3 eV amounts to ≈ 25 m/s. This uncertainty is quite acceptable in comparison to the total broadening of typically several 100 m s^{-1} in this investigation.

4.2. An ensemble of 3D- and ⟨3D⟩-FeH lines

We investigate ten FeH lines between 9950 Å and 9990 Å chosen from Reiners & Basri (2006) (see Tab. 3). We choose lines from different branches (Br), orbital angular momentum ω, and rotational quantum number J. The wavelengths in Tab. 3 are given in vacuum and E_l is the lower transition energy. While not directly relevant in the present context, because we do not study the effects of magnetic fields, we note that five lines are magnetically sensitive and five insensitive. We performed the line synthesis for fixed abundances on the CO^{5}BOLD atmosphere models listed in Tab. 1. The spectral resolution is $R \approx 2 \cdot 10^6$ ($\equiv 5 \cdot 10^{-3}$ Å) corresponding to a Doppler velocity of $v \approx 150$ m s^{-1} at the wavelength of the considered lines (~ 9950 Å). Figures 12 and 13 illustrate the strong influence of surface gravity and effective temperature on the line shape for the 3D-models. In Fig. 12, one can see that for both, ⟨3D⟩- and 3D-lines, the line depth, line width and equivalent width W_λ decrease strongly with increasing effective temperature. The decrease of W_λ is due to stronger dissociation of the FeH molecules at higher temperatures, i.e the number of FeH molecule absorber decreases. Differences in the line shape between 3D- and ⟨3D⟩-lines with changing temperature are hardly visible. To higher T_{eff} values, the influence of broadening on the 3D lines due to velocity fields is slightly visible and not covered by thermal and v.d.Waals broadening anymore. To cooler temperatures, the velocity fields decrease and the differences between the ⟨3D⟩- and 3D-line shapes vanishes. The v.d.Waals broadening is larger then the thermal broadening or that from the small velocity fields in the RHD models. In the model with $T_{\mathrm{eff}} = 2800$ K, the lines start to become saturated. The FeH lines in the z-band at effective temperatures below ~ 2600 K become too saturated and too broad for investigations of quantities like magnetic field strength or rotational broadening below 10 km s^{-1}.

The differences between 3D- and ⟨3D⟩-line shapes of the log g-series in Fig. 13 is more obvious than in the T_{eff} case. The differences in line depth and line width become significant with decreasing log g. The lines in the 3D-models are significantly broadened due to the velocity fields in the RHD models, hence the line width is larger and the line depth lower. As we saw in Chapter 3, these velocity fields increase with decreasing log g and could be described in the 1D case in terms of macro- and micro-turbulent velocities.

The ⟨3D⟩-lines become slightly shallower and narrower towards smaller log g. The equivalent width of the lines decreases with decreasing log g due to decreasing pressure and hence decreasing concentration of of FeH molecules. Also the v.d.Waals broadening looses its influence to lower pressures and the line width decreases. We point out, that we use in all models the same solar like chemical compositions, hence the concentration of Fe and H stays the same. The creation of FeH also depends on the number of H_2-molecules, which become larger towards lower temperatures and will be important in cool models.

The slightly different effective temperatures in the models with different log g (see Tab. 1) affect the line depths as well. If the effective temperatures would be the same in the log g-models, one could expect a monotonic behavior in decreasing line strength for decreasing surface gravity in the ⟨3D⟩-lines. However, because the model with log g = 3.0 is cooler, the line depth is deeper than that of the one with log g = 3.5. In the following analysis we will correct the FWHM, W_λ, and the line depth of the lines on models with different log g for their slightly different effective temperatures.

The ten FeH lines behave all in the same way as the presented ones. We do not see any effect of different excitation potentials or log gf values in the line shapes that cannot be explained by their different height of formation. Thus, we expect that we can exclude an extraordinary interaction between these quantities and effective temperature or surface gravity. We will quantify this preliminary result in the next section.

Table 3. Several quantities of the investigated FeH lines (Reiners & Basri 2006).

| λ_{rest} [Å]	log gf	E_l [eV]	Br.	J	Ω	magn. sen.
9953.08	-0.809	0.156	R	10.5	1.5	weak
9954.00	-2.046	0.199	P	16.5	2.5-3.5	strong
9956.72	-0.484	0.375	R	22.5	3.5	strong
9957.32	-0.731	0.194	R	12.5	1.5	weak
9973.80	-0.730	0.196	R	12.5	1.5	weak
9974.46	-1.164	0.108	R	4.5	0.5	weak
9978.22	-1.190	0.030	Q	2.5	2.5	strong
9979.14	-1.411	0.093	R	2.5	0.5	strong
9981.46	-1.006	0.130	R	6.5	0.5	weak
9982.60	-1.322	0.035	Q	3.5	2.5	strong

4.3. FeH Line shapes

To quantify the visual results of Fig. 12 and Fig. 13, we measured W_λ, the FWHM, and the line depth of the ten investigated FeH-lines (see Tab. 3). We compare 3D- and ⟨3D⟩-lines with each other to study the effects of the velocity fields in the 3D models and to explore the behavior of the FeH without broadening effects from the hydrodynamical motions. A run of these quantities is plotted in Fig. 14 and Fig. 15.

As we mentioned above, we have to correct the line quantities from models with changing log g for their slightly different T_{eff}. In Figs. 12 and 14 one can see how the investigated quantities depend on T_{eff}. We determined spline fits $\wp$ for the three quantities of each line. For these fitting functions $\wp$ we took into account all five different effective temperatures. In order to correct the line quantities to a reference temperature of $T_{\mathrm{eff}}^{\mathrm{Ref.}} = 3275$ K, we use a correction factor $\gamma = \frac{\wp_{\mathrm{quant.}}(T_{\mathrm{eff}}^{\mathrm{Ref.}})}{\wp_{\mathrm{quant.}}(T_{\mathrm{eff}}.)}$ and multiply the quantity for the log g-model with γ. This gives us
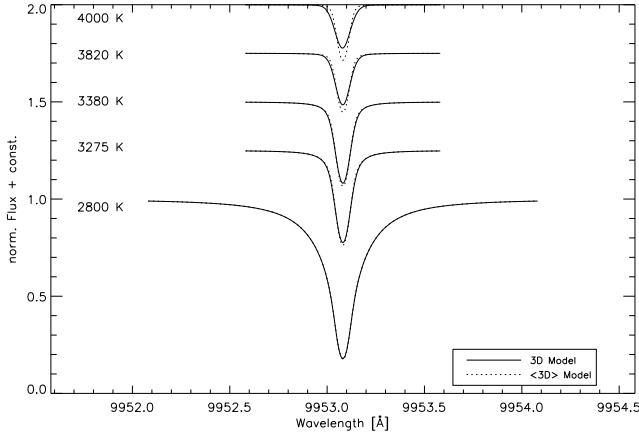
Fig. 12. FeH lines with constant $\log g$ and varying T_{eff}. Plotted are pairs of 3D- and $\langle 3D \rangle$-lines shifted by a constant for better visibility. The models are located at T_{eff} values of 2800 K, 3275 K, 3380 K, 3820 K and 4000 K and a $\log g$ value of 5.0, except the one with $T_{\text{eff}} = 3820$ K ($\log g = 4.9$), and the one with $T_{\text{eff}} = 4000$ K ($\log g = 4.5$) [cgs].
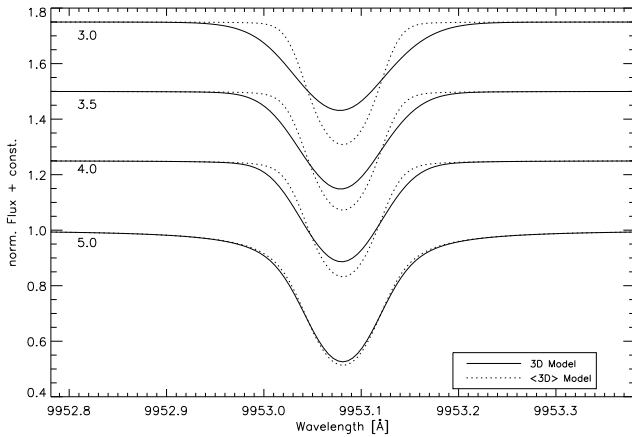

Fig. 13. FeH lines wit constant T_{eff} and varying $\log g$. Plotted are pairs of 3D- and $\langle 3D \rangle$-lines shifted by a constant for better visibility. The models are located at a T_{eff} around $3300K$ and different $\log g$ values of 3.0 ($T_{\text{eff}} = 3240$ K), 3.5 ($T_{\text{eff}} = 3270$ K), 4.0 ($T_{\text{eff}} = 3315$ K) and 5.0 ($T_{\text{eff}} = 3275$ K) [cgs]. The large differences between 3D- and $\langle 3D \rangle$-lines stem from the hydrodynamical velocity fields in the 3D models.

the value of the quantity for a $\log g$-model which would have $T_{\text{eff}} = 3275$ K.

4.3.1. Equivalent Width W_λ

In the T_{eff}-series, W_λ (see Fig. 14 upper panel) decreases with increasing T_{eff}. At higher T_{eff} the number of FeH molecules decrease due to dissociation and hence W_λ. This can be seen in the 3D lines as well as in the $\langle 3D \rangle$-lines. At $T_{\text{eff}} = 2800$ K, the influence of v.d.Waals broadening in the 3D- and $\langle 3D \rangle$-lines becomes clearly visible in the line profile due to saturation of the FeH lines. The ten different FeH lines all behave in a similar manner. The only difference is the absolute value of W_λ, which depends on the $\log gf$-value and excitation potential E_l of each line.
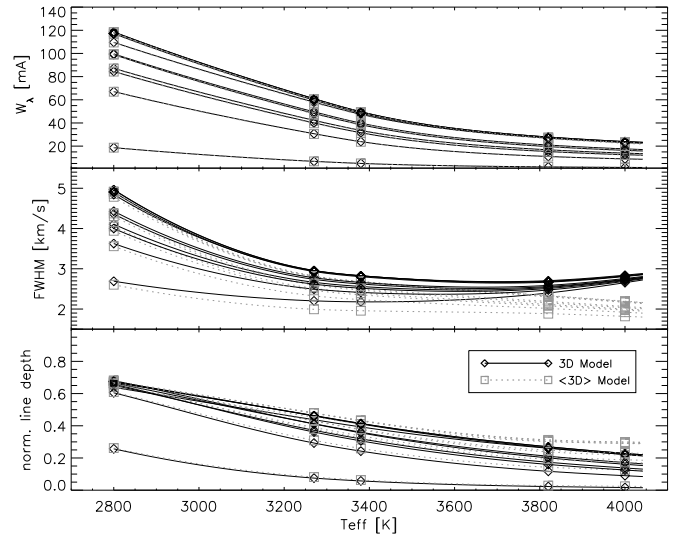

Fig. 14. Run of W_λ (top), FWHM (middle) and the line depth (bottom) of ten FeH-lines (see Tab. 3) on models with different T_{eff}. Squares are the data points for the $\langle 3D \rangle$-models and diamonds for the 3D-models. W_λ and FWHM are on a logarithmic ordinate for better visibility. We connect the data points of each line with fitting functions (see text) to guide the eye. Plotted are the quantities of the 3D-models (black solid lines) and the $\langle 3D \rangle$-models (gray dotted lines). The models are located at T_{eff} values of 2800 K, 3275 K, 3380 K, 3820 K and 4000 K and a $\log g$ value of 5.0, except the one with $T_{\text{eff}} = 3820$ K ($\log g = 4.9$), and the one with $T_{\text{eff}} = 4000$ K ($\log g = 4.5$) [cgs].

In the $\log g$-series, the W_λ (see Fig. 15 upper panel) increases with increasing $\log g$. The change in concentration of FeH with lower $\log g$, which results in smaller W_λ, depends on the changing pressure and density stratification. The difference between
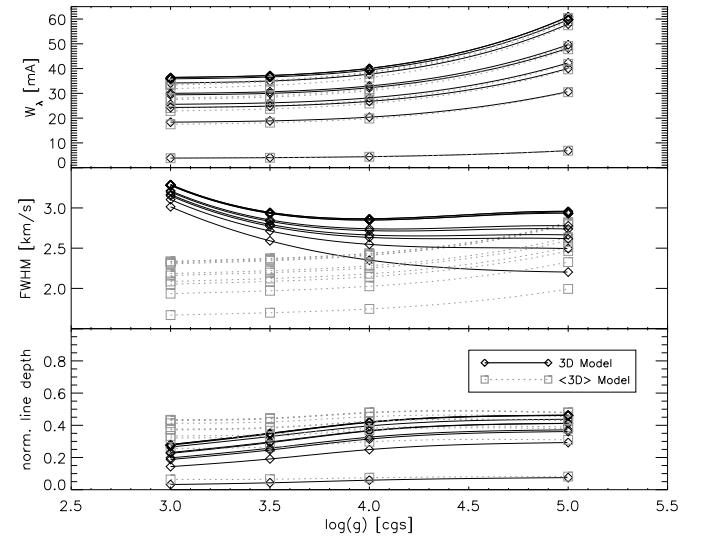
Fig. 15. Run of W_λ (top), FWHM (middle) and line depth (bottom) of ten FeH-lines (see Tab. 3) on models with different $\log g$. Squares are the data points for the $\langle 3D \rangle$-models and diamonds for the 3D-models. We connect the data points of each line with fitting functions (see text) to guide the eye. Plotted are the quantities of the 3D-models (black solid lines) and the $\langle 3D \rangle$-models (gray dotted lines). All quantities are corrected to a T_{eff} of 3275 K.
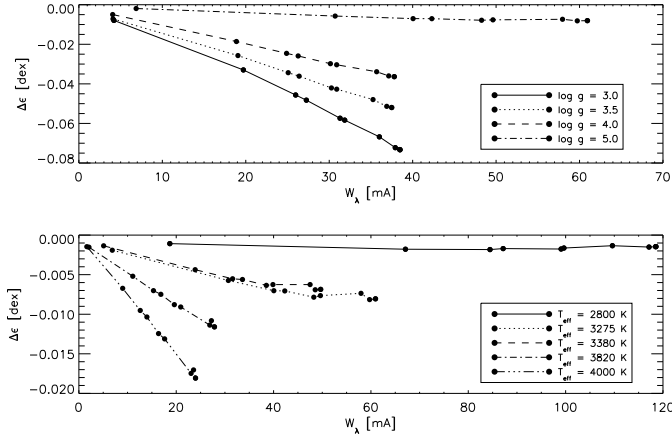
Fig. 16. $3D - \langle 3D \rangle$ corrections to FeH abundances derived from different FeH lines with varying quantities see Tab. 3. Upper panel: The models are located at a T_{eff} around $3300 K$ and different $\log g$ values of 3.0 ($T_{\mathrm{eff}} = 3240$ K), 3.5 ($T_{\mathrm{eff}} = 3270$ K), 4.0 ($T_{\mathrm{eff}} = 3315$ K) and 5.0 ($T_{\mathrm{eff}} = 3275$ K) [cgs]. Lower panel: The models are located at T_{eff} values of 2800 K, 3275 K, 3380 K, 3820 K and 4000 K and a $\log g$ value of 5.0, except the one with $T_{\mathrm{eff}} = 3820$ K ($\log g = 4.9$), and the one with $T_{\mathrm{eff}} = 4000$ K ($\log g = 4.5$) [cgs].

3D- and $\langle 3D \rangle$-lines at small $\log g$-values stems from the broadening by micro-turbulent velocities and vanishes to higher $\log g$ values. This time the FeH lines are only mildly saturated, but the velocity fields in the RHD models (see Sec.3) are strong enough to affect the W_λ as well. Like in the T_{eff}-series, the ten different lines show no significant variations in their behavior. They only vary in the amount of W_λ due to different $\log gf$-values.

Since the differences in W_λ are very small, one can expect that the 3D correction to the FeH abundance is very small too. We derive abundance corrections from comparison between 3D and $\langle 3D \rangle$ curve of growths for each set of lines on the different model atmospheres. The results are plotted in Fig. 16. In this case the correction to the different T_{eff} of the $\log g$ models is not applied. The 3D-$\langle 3D \rangle$ abundance correction is between -0.001 dex for the coolest high $\log g$ model and -0.07 dex for the $\log g = 3.0$ model. In all cases the abundance correction is negative which mean that the 3D lines appear stronger due to the enhanced opacity which becomes larger due to the micro-turbulent velocity.

4.3.2. FWHM

The dependence of the line width (measured as the width of the line at their half maximum (FWHM)) on T_{eff} is shown in the middle panel of Fig. 14. At low T_{eff}, one can see that the FWHM of the 3D- and $\langle 3D \rangle$-FeH lines decreases with increasing T_{eff}. The v.d.Waals broadening loses influence and also the dissociation of FeH molecules leads to smaller and narrower lines. After T_{eff} around 3380 K, the FWHM of the 3D lines reaches a flat minimum and starts to become larger again to higher T_{eff}. This rise in the line width is probably related to the rising velocity fields in the RHD models, since thermal broadening takes place in both, 3D- and $\langle 3D \rangle$-lines and the latter still decrease. The rise of the velocity in the models with a T_{eff} of 3380 K and 4000 K could also be due to the slightly lower surface gravity in these models, but we think that the main influence stems from the higher temperatures. The $\langle 3D \rangle$-lines decrease mono-

tonically with increasing T_{eff} and reflects the behavior of W_λ. The difference in FWHM between 3D- and $\langle 3D \rangle$-lines is very small at $T_{\mathrm{eff}} = 2800$ K and increases with increasing T_{eff} to ~ 0.8 km s^{-1} at the highest T_{eff}. We have seen in Sec.3.2 that this can be explained with the micro- and macro-turbulence description. The offset between the FWHM of the ten lines is due to their different $\log gf$-values i.e. large $\log gf$-values results in large FWHM. But since we are interested in broadening from the velocity fields, we have to take into account that lines with small $\log gf$-values, i.e. weak lines, formed deeper in the atmosphere where the convective motions are stronger. These lines are more broadened from the hydrodynamical velocity fields and hence more widened. We can see in Fig. 14 that the difference in FWHM between the ten 3D lines becomes smaller to high T_{eff}. This is also valid for the lines in the $\log g$-series where the difference in FWHM between the ten 3D lines becomes smaller to small $\log g$-values.

In the $\log g$-series, the dependence of FWHM (Fig. 15 middle panel) is very different for 3D- and $\langle 3D \rangle$-lines. In the 3D case the FWHM stays almost constant with decreasing surface gravity between $\log g$ of 5.0 and 4.0 for most lines. This is due to the smaller amount of v.d.Waals broadening, which loses its influence due to lower pressure in models with smaller surface gravity. This is compared from the broadening due to the rising velocity fields. With $\log g$ smaller than 4.0, the width starts to increase for all lines. This increase of line width in the 3D case is a consequence of the hydrodynamic velocity fields which increase strongly with decreasing $\log g$. In the $\langle 3D \rangle$ case, without the velocity fields, the FWHM decreases with decreasing surface gravity and reflects the behavior of the W_λ. The difference between 3D- and $\langle 3D \rangle$-lines reach its maximal value at $\log g = 3.0$ [cgs] and is around 1.3 km s^{-1}. This is on the order of the velocity fields in the RHD models (see Fig. 8). One could fit 1D spectral synthesis FeH lines to observed ones (with known T_{eff}) with the micro- and macro-turbulence description (see Sec. 3.2) and it will be possible with the obtained velocities to determine a surface gravity with the help of Fig. 11.

We did not see any significant different behavior between the ten FeH lines. Neither in the T_{eff}-series nor in the $\log g$-series.

4.3.3. Line Depth

In the bottom panel of Fig. 14 one can see the dependence of the line depth on T_{eff}. The line depth increases with decreasing T_{eff}, and almost all FeH lines, except the one with the lowest $\log gf$ values are saturated at $T_{\mathrm{eff}} = 2800$ K. The difference in line depth between 3D and $\langle 3D \rangle$-lines is changing in the T_{eff}-interval. At high T_{eff}, the line depth of the $\langle 3D \rangle$-lines is deeper than that of the 3D lines. At $T_{\mathrm{eff}} = 2800$ K, this difference almost vanishes. This behavior is due to the saturation of the FeH lines at low T_{eff} because both, the 3D- and $\langle 3D \rangle$-lines reach their maximal depth. The decrease of the line depth with increasing T_{eff} is due to the dissociation of the FeH molecules at higher temperatures.

The line depth of the $\log g$-series is shown in the bottom panel of Fig. 15. At low $\log g$, the line depths of the 3D and $\langle 3D \rangle$-lines increase almost linearly with increasing $\log g$. The 3D lines increase with a strong slope and the $\langle 3D \rangle$-lines with a weaker slope. The difference in line depth between 3D- and $\langle 3D \rangle$-models is maximal at $\log g = 3.0$ [cgs] and vanishes almost at $\log g = 5.0$ [cgs]. It is consistent with the velocity fields present in the atmospheres of the RHD models broadening the lines and lower the line strength of the 3D lines. The $\langle 3D \rangle$-lines

reflect the decreasing number of FeH molecules with decreasing $\log g$ due to the lower pressures.

5. Summary and Conclusion

We investigated a set of M-star models with T_{eff} = 2500 K - 4000 K and $\log g$ = 3.0 – 5.0 [cgs]. For these models, the 3D hydrodynamic radiative transfer code CO^{5}BOLD was used. The horizontal and vertical velocity fields in the 3D models were described with a binning method. The convective turn-over point is clearly visible in the atmospheric velocity dispersion structure. To investigate the influence of these velocity fields on spectral line shapes, a description for geometrical projection and limb-darkening effects was applied. With the use of contribution functions, we took only these parts in the atmosphere into account where the lines were formed. The resulting velocity dispersions range from 400 – 1600 m s^{-1} with decreasing $\log g$ and with increasing T_{eff} from 200 – 1400 m s^{-1}. These values agree well with velocities deduced from line shapes. We expressed the hydrodynamical velocity fields of the 3D models in terms of the classical micro- and macro-turbulent velocities. With this description and the obtained micro- and macro-turbulent velocities, it is possible to reproduce 3D spectral lines on 1D atmosphere models very accurately, hence time consuming 3D treatment of FeH molecular lines in the regime of cool stars is not necessary for line profile analysis. A comparison of our velocities with a set of velocities determined from observations with spectral fitting methods showed that the macro-turbulent velocities agree, but the micro-turbulent velocities are a factor of two or three smaller than the ones determined from observations.

A line shift due to the larger up-flowing area in the convection zone was investigated too. It is on the order of a few m/s up to 50 m s^{-1} for a very low gravity model. The time dependent jitter in line positions is only about m/s and would be reduced to mm s^{-1} in a real star, due to high number of contributing elements.

In order to use FeH molecular lines for investigations of spectroscopic/physical properties in cool stars (e.g. Zeeman- or rotational broadening), we explored the behavior in a set of lines on $\log g$ and T_{eff}. We investigated ten FeH lines between 9950Å and 9990Å on our models with the spectral synthesis code LINFOR3D. FeH lines react on different effective temperatures as expected due to the change in chemical composition and pressure. The lines showed also a weak dependence on surface gravity due to changing densities and pressure. The broadening from velocity fields in the 3D models of the $\log g$ series is very strong, but for the T_{eff} series the broadening from velocity fields is almost covered by v.d.Waals broadening. The difference in line width for hot models is up to 0.5 km s^{-1} and for low gravity models around 1 km s^{-1}. That means for the 1D spectral synthesis, that one has to include correct micro- and macro-turbulent velocities for small surface gravities or hot T_{eff}. Due to the fact that the FWHM $\log g$ dependence of FeH lines goes in the opposite direction as the $\log g$ dependence of the velocity fields, the FeH lines become a great mean to measure surface gravities in cool stars. Because the velocity fields scale with $\log g$ and it should be easily possible to detect them.

FeH lines with different quantum numbers do not show significant differences for both, $\log g$- and T_{eff}-series. That means the broadening of the lines does not depend on J, Ω, or the branch. Furthermore lines with weak magnetic sensitivity behave just like lines with strong magnetic sensitivity. All lines are broadened in the same way by thermal and hydrodynamical motions. Only the transition probability expressed in the $\log gf$ value influences the behavior of the lines. The line with the lowest gf-values did not saturate at low T_{eff}, but in general they are similar to the other FeH lines.

It is possible to treat the FeH molecular lines with different quantum numbers as homogenous in the absence of magnetic fields. That allows to use FeH lines to measure magnetic fields (Reiners & Basri 2006, 2007). Hence we conclude, that these lines also are an appropriate mean to measure magnetic field strength in M-type stars.

Appendix
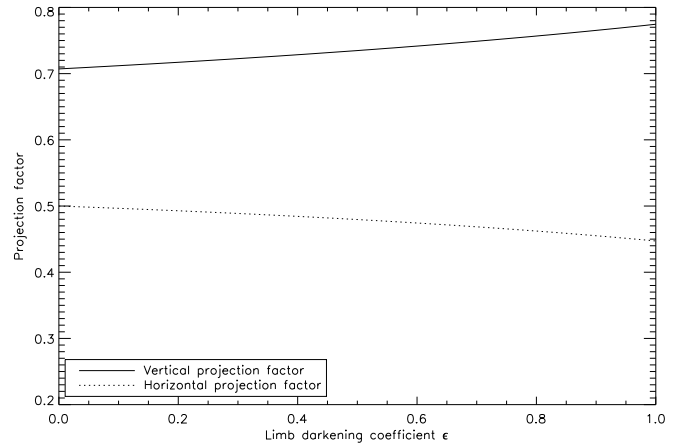
Fig. 17. Projection factors (vertical solid line and horizontal dotted line) as a function of the limb darkening coefficient ϵ.

To compare the hydrodynamical velocity dispersion in 3D-CO^{5}BOLD models with the spectroscopic quantities micro- and macro-turbulent velocities, we assume a simple geometrical model and try to resample the broadening of absorption lines. An intensity beam "sees" the velocity field under a certain angle and the spectral line is broadened by the projection of these velocities. In this sense we project the geometrical velocity components on a line of sight under a certain angle and integrate over all angles in a half sphere. We also take a linear limb-darkening law into account. We assume a velocity function $f(v)$ in velocity space and an intensity line profile

$$I(v) = V(v) \cdot I_c^0 \cdot L(\theta), \tag{2}$$

where $V(v)$ is a line profile function, I_c^0 the continuum intensity at the center of the disk and $L(\theta)$ a limb-darkening law. The integrated flux of the intensity line profile broadened by the velocity function is then given by their convolution and disk integration, i.e.

$$F = \oint f(v) * I(v) \cos\theta \, d\omega, \tag{3}$$

with $d\omega = \sin\theta \, d\theta \, d\phi$, $\phi \in [0, 2\pi]$, $\theta \in [0, \pi/2]$. If we assume that $V(v)$ does not vary with different positions on the disk, it can be factored out (Gray 2008) and

$$F = V(v) * I_c^0 \cdot W(v), \tag{4}$$

with

$$W(v) = \oint f(v) \cdot L(\theta) \cos\theta \, d\omega. \tag{5}$$

With Eq. 5 we are left with a flux-like expression for the velocity function. The dispersion of the velocity function is given by

$$\sigma^2 = \langle f(v)^2 \rangle - \langle f(v) \rangle^2 \tag{6}$$

and we can write for the projected velocity dispersion Σ:

$$\Sigma^2 = \frac{1}{N} \int_0^{2\pi} \int_0^{\pi/2} (\langle (f(v)e)^2 \rangle - \langle f(v)e \rangle^2) \cdot L(\theta) \, \cos\theta \, d\omega \tag{7}$$

where $f(v) = \begin{pmatrix} f_x(v) \\ f_y(v) \\ f_z(v) \end{pmatrix}$ is the velocity vector containing all ve-

locities in a model cube, $e = \begin{pmatrix} \cos\phi \sin\theta \\ \sin\phi \sin\theta \\ \cos\theta \end{pmatrix}$ is the basis vector in

spherical coordinates, and $L(\theta) = 1 - \epsilon + \epsilon \cdot \cos(\theta)$ a linear limb-darkening law with the limb-darkening coefficient ϵ. N is a normalization factor $N = \int_0^{2\pi} d\phi \int_0^{\pi/2} L(\theta) \, \cos\theta \, \sin\theta \, d\theta = \pi(1 - \frac{\epsilon}{3})$. We included the limb-darkening in the normalization because, in opposite to the flux, the velocity dispersion for an isotropic velocity field has to be conserved. The average is taken over the velocities and does not affect the angle dependent parts. Basically we have to integrate:

$$\langle (fe)^2 \rangle - \langle fe \rangle^2 = (\langle f_x^2 \rangle - \langle f_x \rangle^2) \cos\phi^2 \sin\theta^2 +$$
$$(\langle f_y^2 \rangle - \langle f_y \rangle^2) \sin\phi^2 \sin\theta^2 + (\langle f_z^2 \rangle - \langle f_z \rangle^2) \cos\theta^2 +$$
$$2(\langle f_x f_y \rangle - \langle f_x \rangle \langle f_y \rangle) \cos\phi \sin\phi \sin\theta^2 +$$
$$2(\langle f_x f_z \rangle - \langle f_x \rangle \langle f_z \rangle) \cos\phi \sin\theta \cos\theta +$$
$$2(\langle f_y f_z \rangle - \langle f_y \rangle \langle f_z \rangle) \sin\phi \sin\theta \cos\theta. \tag{8}$$

If we want to compute the average of this quantity, we need the mean and the squared mean of the quantities, but not the combinations of the velocity components, because these products vanish in the integration over the half sphere due to their angle dependent coefficients. After the integration of Eq.7, Σ^2 becomes

$$\Sigma^2 = \frac{(\langle f_x^2 \rangle - \langle f_x \rangle^2 + \langle f_y^2 \rangle - \langle f_y \rangle^2)(7\epsilon - 15)}{20(\epsilon - 3)} +$$
$$\frac{(\langle f_z^2 \rangle - \langle f_z \rangle^2)(6\epsilon - 30)}{20(\epsilon - 3)}. \tag{9}$$

We can see, that for an isotropic velocity field $f_x(v) = f_y(v) = f_z(v) = f(v)$ follows that $\sigma^2 = \langle f(v)^2 \rangle - \langle f(v) \rangle^2$ and does not depend on ϵ or the geometrical projection anymore. Setting $\epsilon = 0$, it then follows from Eq. 9 that $\Sigma_{x,y}^2 = \frac{1}{4}\sigma_{x,y}^2$ and $\Sigma_z^2 = \frac{1}{2}\sigma_z^2$ due to geometrical effects.

The projection factors for the vertical $\left(\frac{6\epsilon-30}{20(\epsilon-3)}\right)$ and horizontal $\left(\frac{7\epsilon-15}{20(\epsilon-3)}\right)$ component are plotted as a function of the limb-darkening coefficient ϵ in Fig. 17. They vary only about 5% from no darkening to a full darkened disk. The reduction for the vertical velocity is about 30% and for the horizontal components 50%.

For the sake of completeness, we obtain in a similar way the mean velocities in three spatial directions $\langle f_{x,y,z}(v) \rangle$ which are given by

$$\langle f_{x,y,z}(v) \rangle_{projected} = \frac{1}{N} \int_0^{2\pi} \int_0^{\pi/2} \langle f_{x,y,z}(v)e \rangle \cdot L(\theta) \, \cos\theta \, d\omega. \tag{10}$$

The horizontal velocities vanish due to projection but there is still a vertical component which is reduced to geometrical and limb-darkening effects.

$$\langle f_x(v) \rangle_{projected} = \langle f_y(v) \rangle_{projected} = 0,$$
$$\langle f_z(v) \rangle_{projected} = \frac{(\epsilon - 4)}{2(\epsilon - 3)} \langle f_z(v) \rangle. \tag{11}$$

References

Asplund, M., Grevesse, N., & Sauval, A. J. 2005, in Astronomical Society of the Pacific Conference Series, Vol. 336, Cosmic Abundances as Records of Stellar Evolution and Nucleosynthesis, ed. T. G. Barnes, III & F. N. Bash, 25–+
Barklem, P. S., Piskunov, N., & O'Mara, B. J. 2000, A&AS, 142, 467
Baschek, B., Holweger, H., & Traving, G. 1966, Astronomische Abhandlung der Hamburger Sternwarte, 8, 26
Bean, J. L. 2007, PhD thesis, The University of Texas at Austin
Bean, J. L., Benedict, G. F., & Endl, M. 2006a, ApJ, 653, L65
Bean, J. L., Sneden, C., Hauschildt, P. H., Johns-Krull, C. M., & Benedict, G. F. 2006b, ApJ, 652, 1604
Dravins, D. 1982, ARA&A, 20, 61
Dulick, M., Bauschlicher, Jr., C. W., Burrows, A., et al. 2003, APJ, 594, 651
Ferguson, J. W., Alexander, D. R., Allard, F., et al. 2005, APJ, 623, 585
Freytag, B., Allard, F., Ludwig, H., Homeier, D., & Steffen, M. 2009, A&A, in prep.
Freytag, B., Steffen, M., & Dorch, B. 2002, Astronomische Nachrichten, 323, 213
Gray, D. F. 1975, ApJ, 202, 148
Gray, D. F. 1977, ApJ, 218, 530
Gray, D. F. 2008, The Observation and Analysis of Stellar Photospheres (The Observation and Analysis of Stellar Photospheres, by D.F. Gray. Cambridge: Cambridge University Press, 2008.)
Hauschildt, P. H. & Baron, E. 1999, Journal of Computational and Applied Mathematics, 109, 41
Kurucz, R. L. 1970, SAO Special Report, 309
Ludwig, H. G. 1992, PhD thesis, University of Kiel
Ludwig, H.-G., Allard, F., & Hauschildt, P. H. 2002, A&A, 395, 99
Ludwig, H.-G., Allard, F., & Hauschildt, P. H. 2006, A&A, 459, 599
Ludwig, H.-G., Jordan, S., & Steffen, M. 1994, A&A, 284, 105
Magain, P. 1986, A&A, 163, 135
Nordh, H. L., Lindgren, B., & Wing, R. F. 1977, A&A, 56, 1
Nordlund, A. 1982, A&A, 107, 1
Palla, F. & Baraffe, I. 2005, A&A, 432, L57
Reiners, A. 2007, A&A, 467, 259
Reiners, A. & Basri, G. 2006, ApJ, 644, 497
Reiners, A. & Basri, G. 2007, ApJ, 656, 1121
Sauval, A. J. & Tatum, J. B. 1984, ApJS, 56, 193
Schweitzer, A., Hauschildt, P. H., Allard, F., & Basri, G. 1996, MNRAS, 283, 821
Sneden, C. A. 1973, PhD thesis, AA(THE UNIVERSITY OF TEXAS AT AUSTIN.)
Steffen, M., Ludwig, H.-G., & Freytag, B. 1995, A&A, 300, 473
Vögler, A., Bruls, J. H. M. J., & Schüssler, M. 2004, A&A, 421, 741
Wedemeyer, S., Freytag, B., Steffen, M., Ludwig, H.-G., & Holweger, H. 2004, A&A, 414, 1121
Wilkinson, P. G. 1963, ApJ, 138, 778
Wing, R. F. 1972, in Les Spectres des Astres dans l'Infrarouge et les Microondes, 123–140
Wing, R. F. & Ford, W. K. J. 1969, PASP, 81, 527